

Shear Wave Speed Measurements Using Crawling Wave Sonoelastography and Single Tracking Location Shear Wave Elasticity Imaging for Tissue Characterization

Juvenal Ormachea, *Student Member, IEEE*, Roberto J. Lavarello, *Senior Member, IEEE*, Stephen A. McAleavey, *Member, IEEE*, Kevin J. Parker, *Fellow, IEEE*, and Benjamin Castaneda, *Senior Member, IEEE*

Abstract—Elastography provides tissue stiffness information that attempts to characterize the elastic properties of tissue. However, there is still limited literature comparing elastographic modalities for tissue characterization. This study focuses on two quantitative techniques using different vibration sources that have not been compared to date: crawling wave sonoelastography (CWS) and single tracking location shear wave elasticity imaging (STL-SWEI). To understand each technique's performance, shear wave speed (SWS) was measured in homogeneous phantoms and *ex vivo* beef liver tissue. Then, the contrast, contrast-to-noise ratio (CNR), and lateral resolution were measured in an inclusion and two-layer phantoms. The SWS values obtained with both modalities were validated with mechanical measurements (MM) which serve as ground truth. The SWS results for the three different homogeneous phantoms (10%, 13%, and 16% gelatin concentrations) and *ex vivo* beef liver tissue showed good agreement between CWS, STL-SWEI, and MM as a function of frequency. For all gelatin phantoms, the maximum accuracy errors were 2.52% and 2.35% using CWS and STL-SWEI, respectively. For the *ex vivo* beef liver, the maximum accuracy errors were 9.40% and 7.93% using CWS and STL-SWEI, respectively. For lateral resolution, contrast, and CNR, both techniques obtained comparable measurements for vibration frequencies less than 300 Hz (CWS) and distances between the push beams (Δx) between 3 mm and 5.31 mm (STL-SWEI). The results obtained in this study agree over an SWS range of 1–6 m/s. They are expected to agree in perfectly linear, homogeneous, and isotropic materials, but the SWS overlap is not guaranteed in all materials because each of the three methods have unique features.

Index Terms—Crawling wave sonoelastography (CWS), elastography, single tracking location shear wave elasticity imaging (STL-SWEI), tissue characterization.

I. INTRODUCTION

ELASTOGRAPHY is a technique that attempts to characterize the elastic properties of tissue in order to provide additional and more useful information for clinical diagnosis [1], [2]. Several elastographic techniques, mostly based on ultrasound but also on magnetic resonance imaging and optical coherence tomography, have been proposed and applied to a number of clinical applications such as cancer diagnosis (prostate, breast, liver), hepatic fibrosis staging, early detection of renal pathology, focal thyroid lesion characterizations, and others [1], [2].

Particular attention has focused on the measurement of liver stiffness as a stage discriminator for chronic liver disease [3]–[5]. Transient elastography (TE) is a widely used and validated noninvasive method for assessing liver fibrosis [4], [5]. For example, TE appears to be reliable for the detection of significant fibrosis or cirrhosis in hepatitis B patients [6]. However, it is less applicable in the clinic than serum biomarkers particularly in the case of ascites, obesity, and limited operator experience [7]. Other elastographic modalities have been applied in liver studies. Zhang *et al.* [8] concluded that acoustic radiation force impulse imaging (ARFI) may be a reliable method for diagnosing the stage of liver fibrosis with a similar predictive value as TE. In [9], supersonic shear imaging (SSI) is an efficient method for assessing liver fibrosis, comparing favorably with TE and ARFI. These studies compare their results in terms of the propagating shear wave speed (SWS) in the liver tissue; however, TE estimates the SWS typically at 40–50 Hz [5] and ARFI or SSI measure the SWS at a frequency range between 100 and 500 Hz [5], [10], [11]. Therefore, a further comparison study to understand SWS estimation in different elastographic modalities is necessary and important for tissue characterization.

Recently, Oudry *et al.* [12] measured elastic properties using different quantitative modalities in

Manuscript received March 17, 2016; accepted May 31, 2016. Date of publication June 6, 2016; date of current version September 12, 2016. This work was supported in part by the Fondos para la Innovación Ciencia y Tecnología-PERU under Grant 205-FINCYT-IA-2013, and in part by the Fondo Nacional de Desarrollo Científico y Tecnológico-PERU under Grant 012-2014-FONDECYT-C1 and Grant 213-2014-FONDECYT. This work was also supported by the University of Rochester Hajim School of Engineering and Applied Sciences.

J. Ormachea and K. J. Parker are with the Department of Electrical and Computer Engineering, University of Rochester, Rochester, NY 14627 USA (e-mail: jormache@ur.rochester.edu; kevin.parker@rochester.edu).

R. J. Lavarello and B. Castaneda are with the Departamento de Ingeniería, Sección de Electricidad y Electrónica, Pontificia Universidad Católica del Perú, Lima 32, Peru (e-mail: lavarello.rj@pucep.edu.pe).

S. A. McAleavey is with the Department of Biomedical Engineering, University of Rochester, Rochester, NY 14627 USA (e-mail: stephen.mcaleavey@rochester.edu).

Digital Object Identifier 10.1109/TUFFC.2016.2576962

tissue-mimicking phantoms. Their results suggest a bias in elastic property estimation, which varies with each quantitative modality and highlights the difficulty in finding a reference method to assess the elastic properties. In [13] and [14], interlaboratory studies of SWS estimation were performed in elastic and viscoelastic phantoms, respectively. These studies found a significant difference among measurements at different depths. Similar to [12], their results suggest that there is a component of variance attributed to the different measurement systems.

The aforementioned comparison studies of quantitative elastographic methods contribute to the validation and standardization of different elastographic techniques. Nevertheless, there is still a lack of studies comparing 2-D quantitative elastographic techniques being actively developed and applied in soft tissues based on mechanically vibrating external forces (such as vibroelastography [15] or crawling wave sonoelastography (CWS) [16]) and 2-D quantitative elastographic techniques based on acoustic radiation force (such as comb-push ultrasound shear elastography (CUSE) [17] or single tracking location shear wave elasticity imaging (STL-SWEI) [18]). This study focuses on the comparison between two quantitative techniques that are different in excitation source (external versus ARFI), in frequency range (lower versus higher), and in bandwidth (narrowband versus broadband), that have not been compared in the past: CWS and STL-SWEI, so agreement is not guaranteed. The estimations of SWS, contrast, contrast-to-noise ratio (CNR), and spatial resolution are compared in pure elastic gelatin-based homogeneous phantoms, an inclusion phantom, and a two-layer phantom. Additionally, the SWS is compared using both modalities in *ex vivo* beef liver tissue, a viscoelastic material. The SWS values obtained with both modalities are validated with mechanical measurements (MM), which serve as a ground truth. The rest of the document is organized as follows. Section II introduces the materials for the experiments and the methods for the SWS, contrast, CNR, and spatial resolution estimation. Section III presents the experimental results. Section IV contains the discussion of our experimental results. Finally, Section V presents the conclusions.

II. MATERIALS AND METHODS

All the experiments were performed at laboratory temperatures (LT) (16 °C–17 °C) and on the same day to avoid changes in the phantom or tissue materials. Temperature was confirmed using a thermometer (model 87V, Fluke Corp., Everett, WA, USA) whose reader (2 mm diameter) was placed inside and close to the field of view in each scanned media. The mechanical testing and ultrasound scans were made in three different laboratories at the University of Rochester. Fig. 1 shows the geometry of each phantom and the setup for the MM, CWS, and STL-SWEI techniques.

A. Homogeneous, Inclusion, and Two-Layer Phantoms

Homogeneous phantoms were constructed following the procedure used by Hah *et al.* [19]. Three different phantoms with gelatin (300 Bloom Pork Gelatin, Gelatin Innovations

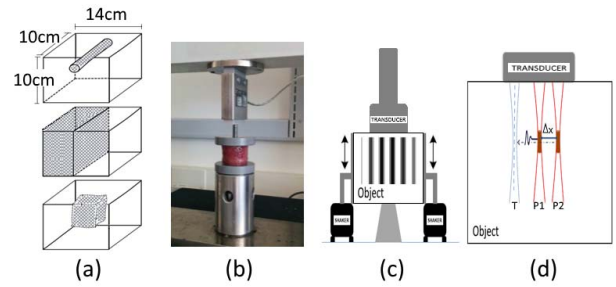


Fig. 1. (a) Phantom geometry representation for the inclusion and two-layer phantoms, and the *ex vivo* beef liver tissue embedded in gelatin, top to the bottom, respectively. (b) MM, (c) CWS, and (d) STL-SWEI schematic setups.

Inc., Schiller Park, IL, USA) concentrations of 10%, 13%, and 16% were created by heating a mixture of gelatin, 1.8 l of degassed water, 16.2 g of Na-Cl, 36 g of graphite, and 2.7 g of agar to 50 °C. The mixture was then cooled to approximately 30 °C and poured into a cubic mold (14 × 10 × 10 cm³) and was then allowed to rest at 4 °C overnight. Additionally, two different phantoms were created using the same materials and procedure described previously. Each of them has two distinct regions: one with gelatin concentration of 13%, and 10%. The first phantom consisted of a stiffer cylindrical inclusion, 12.6 mm in diameter, embedded in an otherwise homogeneous background (inclusion phantom). The second was a two-layer phantom (one region softer than the other). Before subsequent experiments were performed, these phantoms were taken out of the molds and left at LT for 3 h.

B. Ex Vivo Beef Liver Tissue

Five fresh and normal beef liver specimens were acquired and used for this study. A square-shaped sample (5 × 4 × 3 cm³) was extracted from each beef liver and suspended in a cube-shaped mold (14 × 10 × 10 cm³). An 8% gelatin mixture, heated to 50 °C and subsequently cooled to 30 °C, was poured into the mold following the same procedure used by Barry *et al.* [20]. Then, the solid gelatin phantom was removed from the mold and allowed to rest at LT for 10 min prior to scanning. The *ex vivo* beef liver tissue is embedded in gelatin as a practical step to ensure acoustical and shear wave coupling for any surface, as has been performed previously in [5] and [19]–[21].

C. Mechanical Measurements

For each physical phantom, stress relaxation tests were performed on three cylindrical samples (approximately 38 mm in diameter and 33 mm in length) made with the same mixture used to construct the gelatin-based media. For each beef liver, cylindrical samples (approximately 30 mm in diameter and 38 mm in length) were acquired using a custom-made coring knife. Eight cylindrical samples were carefully selected to avoid large-scale vessels or ligaments. The samples were stored in normal (0.9%) saline until mechanical tests were performed using the procedure described by Zhang *et al.* [22]. A QT/5 mechanical device (MTS Systems Co., Eden Prairie, MN, USA) with a 5-N load cell was used to test the samples.

The compression rate and the strain value were adjusted to 0.5 mm/s and 5%, respectively. These parameters were used to set a sufficient loading. Moreover, the strain selected is a common compressive value used by other authors which has produced consistent results [22], [23]. The tests lasted approximately 700 s. MM were considered the reference when assessing the accuracy of the elastographic measurements. Similar to [22] and [24], the stress relaxation curve of each sample was fitted to the Kelvin–Voigt Fractional Derivative (KVFD) model using standard nonlinear least squares procedures. The averaged model parameters, E_0 , η , and α (E_0 , is the relaxed elastic constant, η is the viscoelastic parameter, and α is the order of fractional derivative), were then used to estimate the SWS at any frequency. For all measurements, only curve fitting with a correlation coefficient value larger than 0.97 was included in order to demonstrate that the KVFD model is appropriate for this study. The full mathematical description of the KVFD model can be found in [22].

D. Shear Wave Speed Estimation Using Crawling Wave Sonoelastography

An amplifier (model 5530, AE Techron, Elkhart, IN, USA) driven by a dual channel function generator (model AFG3022B, Tektronix, Beaverton, OR, USA) provided input signals to two mechanical vibration sources (Bruel & Kjaer, Naerum, Denmark) vibrating at low frequencies—40–280 Hz for beef liver tissue and 160–500 Hz for phantoms—and placed at opposite sides of the phantoms. Using these sources, vibrations were applied to generate a relatively uniform vibration field. A GE LOGIQ 9 ultrasound system (GE Healthcare, Wauwatosa, WI, USA) was used to perform sonoelastographic imaging with a linear array (M12L, GE Healthcare, Wauwatosa, WI, USA) positioned between the vibration sources. The center frequency was 5 MHz and the tracking pulse repetition frequency range was 0.240–1.068 kHz. An $F/\#$ of 3 was used for tracking and an $F/\#$ of 1.5 was used for dynamic receive. To estimate the SWS, the crawling wave signal phase was extracted using the method described in [19] and [21]

$$c_s(f) = \frac{2\pi f v}{\theta'(x)} \quad (1)$$

where f_v is the vibration frequency and $\theta(x)$ is the unwrapped phase of the crawling wave signal. The phase was obtained by taking the Fourier transform of each pixel projection over the time axis from the crawling wave image.

CWS has been applied to detect radio frequency ablated hepatic lesions *in vitro* [25], to characterize human skeletal muscle *in vivo* [26], to characterize human prostate tissue *ex vivo* [27], and to evaluate shear wave dispersion in liver steatosis [20].

E. Shear Wave Speed Estimation Using Single Tracking Location Shear Wave Elasticity Imaging

A Siemens Antares scanner (Siemens Medical Solutions, Malvern, PA, USA) and a Siemens Antares VF7-3 linear array transducer (Siemens Medical Solutions, Malvern, PA, USA),

were used to generate pushing beams as well as to track the induced displacements. This equipment was used in previous studies for gelatin phantoms and *ex vivo* liver tissue applications [18], [28], [29]. The center frequency of both the push and track pulses was 4.21 MHz, the acoustic radiation force excitation was 200 μ s and the tracking pulse repetition frequency was 7.44 kHz. An $F/\#$ of 3.5 was used for ARFI excitation, an $F/\#$ of 2 was used for tracking, and an $F/\#$ of 0.75 was used for dynamic receive. In the STL-SWEI algorithm, the acoustic radiation force was applied at two locations, $P1$ and $P2$, and the induced shear waves were tracked at one location, T , 7.08 mm from $P1$ [see Fig. 1(d)]. The distance between the pushing pulses, Δx , was varied between 2.66 and 6.20 mm, to evaluate how Δx influences the lateral resolution, contrast, and CNR estimation in phantoms. For the beef liver tissue study, shorter distances between T and $P1$ (4.06 mm) and $P1$ and $P2$ (3.04 mm) were used due to higher shear wave attenuation. Then, the SWS can be estimated using

$$c_s = \frac{\Delta x}{\Delta t} \quad (2)$$

where Δx is the distance between $P1$ and $P2$, and Δt is the arrival time difference between the two observed shear wave signals.

STL-SWEI has been applied in phantoms and excised porcine liver tissue [28], [30], and to estimate the viscoelastic parameters of *ex-vivo* bovine liver [18], [29].

If we model the push pulse and resulting shear waves as cylindrical spreading, then plane wave relations are not accurate close to the source and at low frequencies. For example, (2) assumes plane wave behavior and thus, a spatial dependence on the phase $k_s \Delta x$ (where k_s is the wavenumber). This approximation holds for large $k_s \Delta x$ [31]. In order to know the corresponding frequency range of the SWS using STL-SWEI, the phase difference between [31, eq. (15)] (which considers cylindrical shear wave behavior) and the plane wave phase shift was compared, that is

$$r = \frac{\mathcal{L}\{H_0^{(1)}(k_S \Delta_{TP1}) \overline{H_0^{(1)}(k_S \Delta x)}\}}{\mathcal{L}\{e^{k_s(\Delta_{TP1} - \Delta x)}\}} \quad (3)$$

where the overline indicates the complex conjugate, Δ_{TP1} is the distance between T and $P1$, H_0^1 is the zeroth-order Hankel function of the first kind. Then, r was arbitrarily chosen between 0.975 and 1, in order to obtain the corresponding frequency range of STL-SWEI.

Therefore, a comparison between the SWS values obtained using CWS and STL-SWEI can be presented for a range of frequencies and validated with MM.

F. Lateral Resolution Estimation

The lateral resolution was estimated by fitting the average SWS profile across the inclusion phantom with a double sigmoid function that models the background-inclusion-background profile shape [32], that is

$$c(x) = (c_{in} - c_{out}) \left(\frac{1}{1 + e^{\frac{x_1 - x}{\lambda_1}}} \right) \left(\frac{1}{1 + e^{\frac{x - x_2}{\lambda_2}}} \right) + c_{out} \quad (4)$$

where x is the lateral position, c_{in} and c_{out} are the SWS in the inclusion and background, respectively, x_1 and x_2 are the locations of the inclusion boundaries, and λ_1 and λ_2 represent the widths of the transition from the background into the inclusion, and from the inclusion into the background, respectively. For the two-layer phantom, the term $(1/1 + e^{x-x_2/\lambda_2})$ in (4) is not considered. The six parameters (c_{in} , c_{out} , x_1 , x_2 , λ_1 , λ_2) were estimated using a standard nonlinear least squares fitting procedure. The estimation of λ_1 and λ_2 enable the measurement of the SWS resolution R_{2080} , defined as the distance required for a 20%–80% transition of the SWS [32], to be evaluated quantitatively as

$$R_{2080,i} = 2\ln(4)\lambda_i$$

$$i = \begin{cases} 1, & \text{for the two layer phantom} \\ 1 \text{ and } 2, & \text{for the inclusion phantom.} \end{cases} \quad (5)$$

G. Contrast and CNR Estimation

The contrast and CNR were evaluated in the SWS images from the inhomogeneous phantoms using

$$\text{Contrast} = \frac{|\bar{c}_{in} - \bar{c}_{out}|}{\bar{c}_{out}} \quad (6)$$

$$\text{CNR} = \frac{|\bar{c}_{in} - \bar{c}_{out}|}{\sqrt{\sigma_{in}^2 + \sigma_{out}^2}} \quad (7)$$

where \bar{c}_{in} and \bar{c}_{out} are the mean values of the SWS at rectangular regions within the inclusion and background regions, respectively, and σ_{in} and σ_{out} are the standard deviation for the same regions, respectively.

III. RESULTS

A. Shear Wave Speed Estimation in Homogeneous Phantoms

Fig. 2 shows shear waves images estimated with CWS (left column) and STL-SWEI (right column) for a 10% gelatin phantom [Fig. 2(a) and (b)], 13% [Fig. 2(c) and (d)], and 16% [Fig. 2(e) and (f)]. For all cases, a CWS image estimated using a 380 Hz vibration frequency (ν_f) and an STL-SWEI image using Δx equal to 4.43 mm are displayed for comparison purposes. Subsequently, a region of interest ($1.5 \times 1.0 \text{ cm}^2$) was extracted from the center of each image to obtain the SWS and its standard deviation.

Fig. 3 shows the comparison plots of SWS as a function of frequency using CWS, STL-SWEI, and MM for all phantoms. In CWS, the maximum accuracy errors obtained were 2.52%, 1.63%, and 2.26% for the 10%, 13% and 16% gelatin phantoms, respectively, at 160 Hz. In STL-SWEI, better agreement compared with MM was obtained at a higher frequency range than was used for CWS. The estimated frequency range, using (3), for the 10%, 13%, and 16% phantoms were 380–860 Hz, 420–1060 Hz, and 460–1200 Hz, respectively. The maximum accuracy errors obtained were 2.22% at 380 Hz, 2.35% at 420 Hz, and 0.71% at 460 Hz for the 10%, 13% and 16% gelatin phantom, respectively. It can be noted that since the phantoms consist of almost purely elastic material, the dispersion results (relationship between SWS-frequency) remains almost constant for the entire frequency range. In that

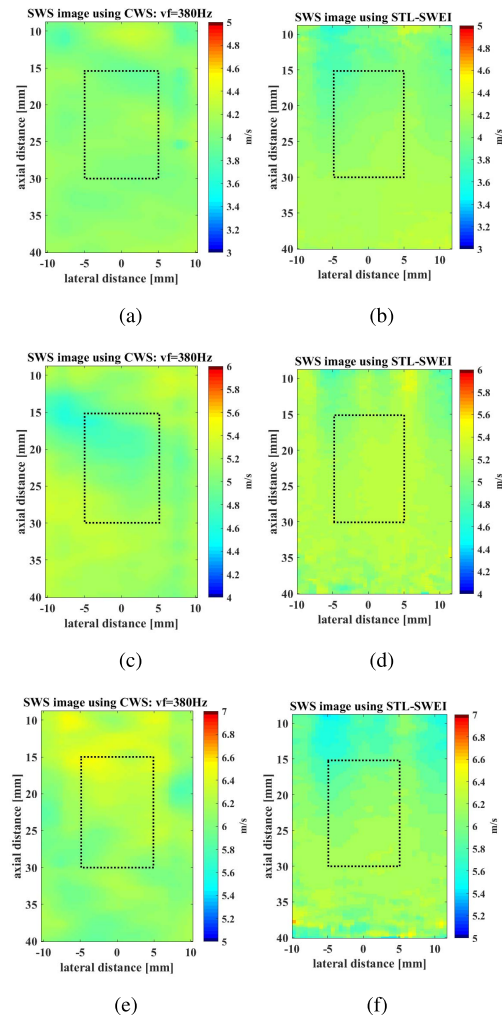


Fig. 2. SWS maps estimated with CWS (left column) and STL-SWEI (right column) for (a) and (b) 10%, (c) and (d) 13%, and (e) and (f) 16% gelatin phantom. The CWS images correspond to 380 Hz vibration frequency and Δx equals 4.43 mm. The black square illustrates the region of interest extracted for all images.

sense, for each technique and phantom, all the averaged SWS measurements between 460–500 Hz were combined to perform a statistical test. The Tukey–Kramer test showed that the SWS measurements, obtained with each modality, are not significantly different ($p > 0.05$) for the same phantom type (see Fig. 4). Additionally, the test showed that each modality is able to differentiate the elastic material properties, the SWS results for each phantom were significantly different ($p < 0.05$) (10% versus 13% versus 16%). Table I indicates the p value obtained for different compared materials.

B. Shear Wave Speed Estimation in the Two-Layer and Inclusion Phantoms

The SWS images estimated by CWS for the two-layer and inclusion phantoms are presented in Figs. 5 and 7, respectively. Similarly, Figs. 6 and 8 show the SWS images estimated by STL-SWEI for the two layer and inclusion phantom, respectively. It is worth noting that Figs. 5–8 do not correspond exactly to the same scanning position because

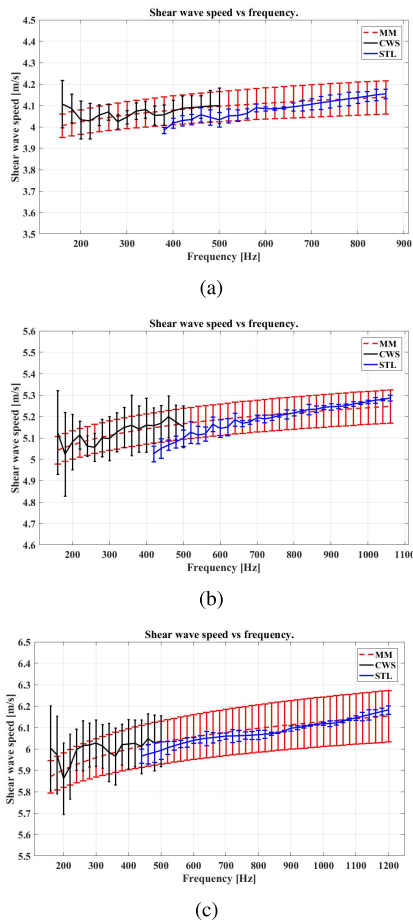


Fig. 3. Comparison plots of CWS, STL-SWEI, MM using the KFVD model for (a) 10%, (b) 13%, and (c) 16% gelatin phantom.

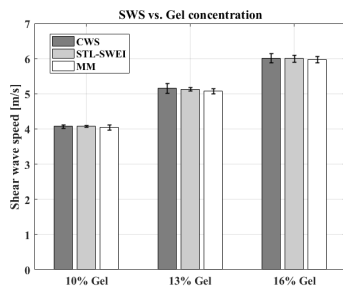


Fig. 4. Aggregate SWS measurements between 460 and 500 Hz for each modality and phantom. The error at each bar corresponds to the standard deviation of the SWS mean values at the aforementioned frequency range. SWS results for each phantom were significantly different ($p < 0.05$) (10% versus 13% versus 16%).

TABLE I

p VALUE OBTAINED FROM STATISTICAL TESTING

Modalities	Compared materials	Frequency [Hz]	p
CWS/STL-SWEI/MM	10 % Gel-phantom	460-500	0.052
CWS/STL-SWEI/MM	13 % Gel-phantom	460-500	0.063
CWS/STL-SWEI/MM	16 % Gel-phantom	460-500	0.060
CWS/STL-SWEI/MM	<i>ex vivo</i> beef liver	200	0.123

the CWS and STL-SWEI images were derived from different data sets obtained with different scanners. Nevertheless, all of them are able to contribute to the estimation of lateral

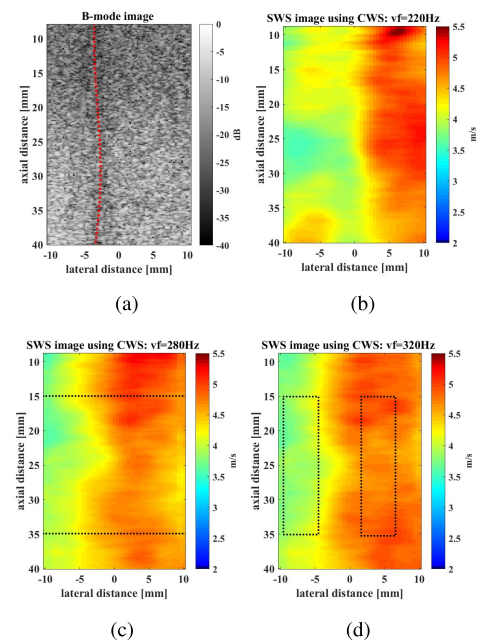


Fig. 5. (a) B-mode image of the two layer phantom. Red dotted line: boundary between the softer and stiffer region. (b)–(d) SWS images obtained with CWS for 220, 280, and 320 Hz, respectively. Black dotted lines in (c) indicate the region used to obtain the average SWS profile in the axial direction. Black dotted rectangles in (d) show the regions used to estimate the contrast and CNR.

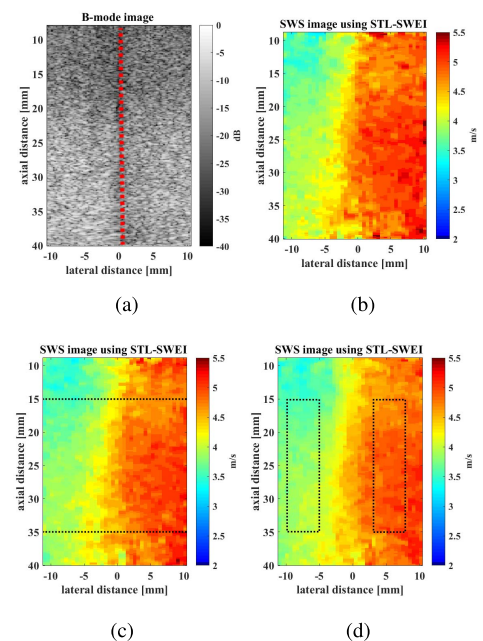


Fig. 6. (a) B-mode image of the two layer phantom. Red dotted line: boundary between the softer and stiffer region. (b)–(d) SWS images obtained with STL-SWEI for Δx equal to 3.54, 4.43, and 6.2 mm, respectively. Black dotted lines in (c) indicate the region used to obtain the average SWS profile in the axial direction. Black dotted rectangles in (d) show the regions used to estimate the contrast and CNR.

resolution, contrast, and CNR. Figs. 5 and 7 show the SWS images obtained using CWS at different vibration frequencies. Figs. 6 and 8 present the SWS images obtained using STL-SWEI for different Δx values (3.54, 4.43, and 6.2 mm).

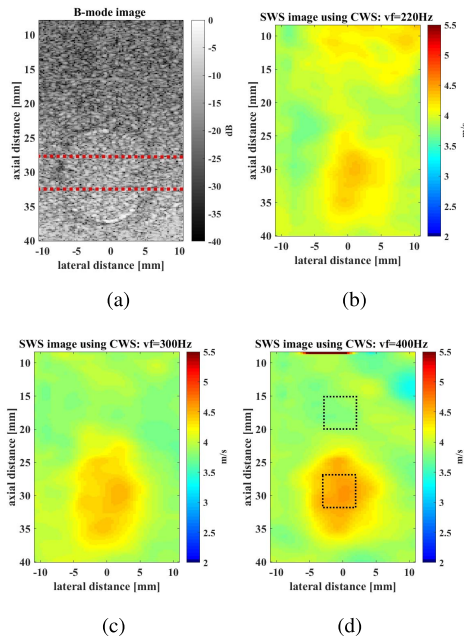


Fig. 7. (a) B-mode image of the inclusion phantom. Red dotted lines in (a) indicate the region used to obtain the average SWS profile in the axial direction. (b)–(d) SWS images obtained with CWS for 220, 300, and 400 Hz, respectively. Black dotted squares in (d) show the regions used to estimate the contrast and CNR.

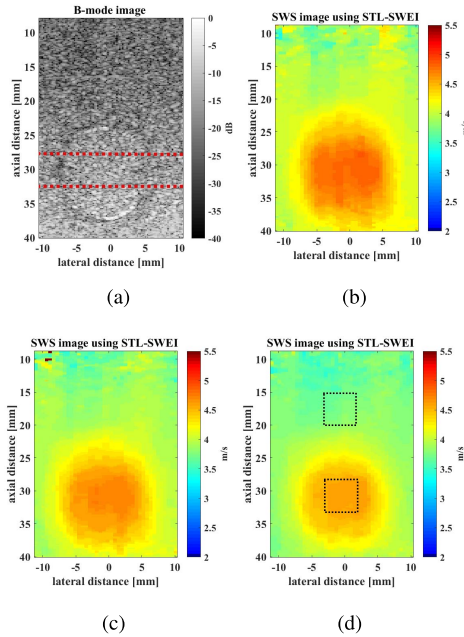


Fig. 8. (a) B-mode image of the inclusion phantom. Red dotted lines in (a) indicate the region used to obtain the average SWS profile in the axial direction. (b)–(d) SWS images obtained with STL-SWEI for Δx equal to 3.54, 4.43, and 6.2 mm, respectively. Black dotted squares in (d) show the regions used to estimate the contrast and CNR.

C. Lateral Resolution Results

The lateral resolution was evaluated using the criteria described in Section II-F. For both cases (CWS and STL-SWEI), good agreement was obtained when fitting the SWS profile across a region of interest for both types of two layer and inclusion phantoms with their corresponding

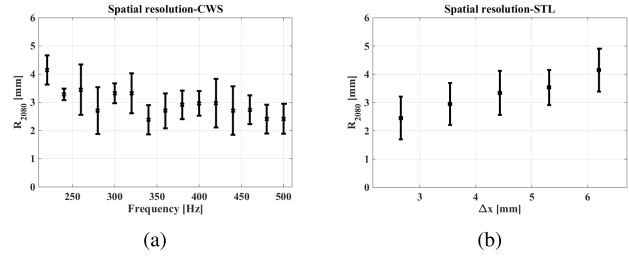


Fig. 9. Lateral resolution estimation. (a) Lateral resolution versus frequency using CWS. (b) Lateral resolution versus Δx using STL-SWEI.

sigmoid or double sigmoid functions (i.e., correlation coefficients larger than 0.97 for all cases). Thus, no uncertainties due to the applied model were considered. Using (5), one or two R_{2080} values for the two layer and inclusion phantoms were calculated. For all cases, the average between $R_{2080,1}$ and $R_{2080,2}$ was obtained. The lateral resolution results versus frequency for the CWS experiments is shown in Fig. 9(a). It was found that the lateral resolution ranged between 4.19 ± 0.52 and 2.38 ± 0.51 mm for a frequency range from 220 to 500 Hz. The frequency range used for the resolution estimation was the same as that used for homogeneous phantoms. However, lateral resolution estimation using vibration frequencies lower than 220 Hz were not as accurate as we expected. This could be because at lower frequencies, CWS has longer interference fringe spacing, and thus the difficulty in differentiating targets increases. The lateral resolution versus Δx derived from the STL-SWEI images is shown in Fig. 9(b). It was found that the lateral resolution estimation ranged between 2.45 ± 0.75 mm and 4.15 ± 0.73 mm. This resolution range is comparable to the one obtained with CWS. As shown, as the Vf increases for CWS or Δx decreases for STL-SWEI, better lateral resolution could be obtained. These results were as expected.

D. Contrast and CNR Results

For contrast and CNR estimation, we selected two different regions of the same size (2×0.5 cm² for the two layer phantom and 0.5×0.5 cm² for the inclusion phantom). Although it would be better to locate these regions at the same depth as shown in Figs. 5(d) and 6(d), it was not possible to choose reasonable regions of the same size at the same depth in Figs. 7 and 8 due to the size of the inclusion. Nevertheless, the mean SWS measured inside the chosen background region presents variations of less than 3% compared with the mean SWS obtained at lateral regions in the inclusion. Figs. 7(d) and 8(d) show the chosen regions located at positions similar to other studies [17], [25]. The contrast for both elastographic techniques is reported in Fig. 10(a) and (b). Contrast values for CWS were in the range of 0.13 ± 0.03 to 0.23 ± 0.01 , and in the case of STL-SWEI, the contrast was in the range of 0.19 ± 0.02 to 0.22 ± 0.02 . Fig. 10(a) shows that as the Vf increases, the contrast approaches 0.25. Fig. 10(b) shows that contrast values estimated with STL-SWEI tend to decrease as Δx increases. This result may be due to the fact that the estimated SWS is an average of the region between the push beams. The CNR obtained with both techniques is shown in Fig. 11(a) and (b). In this case,

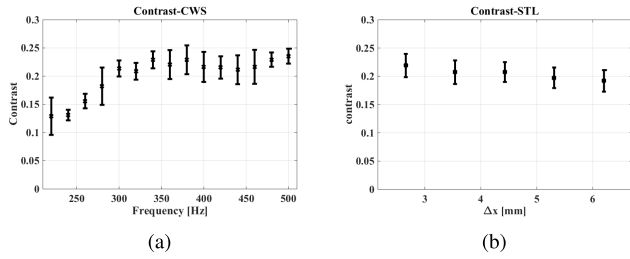


Fig. 10. (a) Contrast versus frequency using CWS. (b) Contrast versus Δx using STL-SWEI.

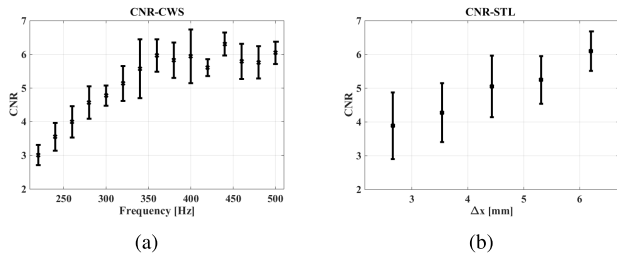


Fig. 11. (a) CNR versus frequency using CWS. (b) CNR versus Δx using STL-SWEI.

the CNR ranges between 3.01 ± 0.29 and 6.31 ± 0.33 for CWS and 3.88 ± 0.98 and 6.09 ± 0.58 for STL-SWEI. In the latter case [see Fig. 11(b)], the CNR results present higher standard deviations values compared with the CWS-CNR results.

E. Shear Wave Speed Estimation in Ex Vivo Beef Liver Tissue

Similar to the previous gelatin phantom experiment, the same region of interest was selected to obtain the SWS average and its standard deviations. The SWS results are, generally, in the range of 1.0–2.0 m/s, which is similar to the values obtained in animal livers [33]–[35]. The estimated frequency range, considering (3), for the *ex vivo* beef liver using STL-SWEI were 120–380 Hz, which is in agreement with a typical frequency range for soft tissues [36]. It should be noted that the frequency range differs from that used for phantom experiments due to higher shear wave attenuation.

Fig. 12 shows the comparison plots of SWS as a function of frequency using CWS, STL-SWEI, and MM for an *ex vivo* beef liver experiment. Table II presents the accuracy errors with respect to MM using CWS and STL-SWEI. The maximum accuracy error estimated using CWS was 9.40% at 40 Hz. The maximum accuracy error for STL-SWEI was 7.93% at 120 Hz. As noted in Section II-E, the lower frequency in STL-SWEI is related to the minimum value of r . The Tukey–Kramer test showed that the three modalities are not significantly different ($p > 0.05$) for each frequency corresponding to the overlapping frequency range (120–280 Hz).

IV. DISCUSSION

A. SWS and Accuracy Estimation in Phantoms

Both techniques, CWS and STL-SWEI, were able to estimate SWS at their corresponding frequency range. Furthermore, it was possible to obtain a close correspondence among the three modalities. As it can be observed, CWS has better

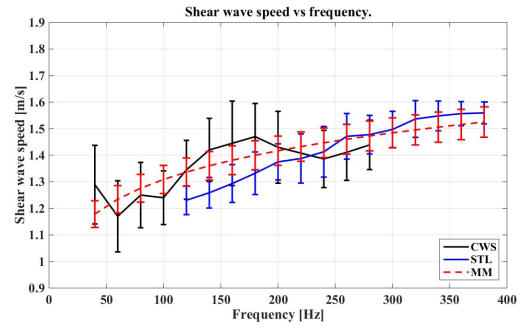


Fig. 12. Comparison plots of CWS, STL-SWEI, and MM using the KFVD model for a beef liver experiment.

TABLE II
SWS ERROR WITH RESPECT TO MM USING CWS AND STL-SWEI
FOR *Ex Vivo* LIVER TISSUE [%]

Method	Frequency [Hz]									
	40	100	120	140	160	180	240	280	340	380
CWS	9.40	5.26	0.63	4.39	4.61	5.00	3.25	1.45	—	—
STL-SWEI	—	—	7.93	7.45	6.35	4.85	3.14	0.75	2.75	2.25

accuracy than STL-SWEI, with respect to MM, for lower frequencies. Although it was expected that CWS achieve a better SNR, boundary reflections, and limited field of view increase the variability in the measurements obtained using this method. In addition, the combination of lower frequencies and stiffer materials provides the worst conditions for SWS estimation using CWS. For STL-SWEI, good correlation was obtained with MM results for a higher frequency range than CWS. In STL-SWEI, in order to obtain the SWS versus frequency data, a plane wave propagation behavior was considered as explained in Section II-E for the shear waves generated by the two pushes. More details on the estimation of mechanical properties using STL-SWEI can be found in [18] and [29]. The accuracy error results, for all gelatin phantoms, demonstrate that the range of r in (3) is a reasonable criteria applied in this study. However, if the lowest value of r decreases, i.e., $r < 0.975$, a larger frequency range may be obtained, but a higher accuracy error at lower frequencies would result. As shown, CWS cannot be used at higher frequencies due to the presence of higher attenuation across the large ROI. Although the shear waves generated in STL-SWEI are also attenuated, they are tracked close to the place where the acoustic radiation force was applied and therefore allow the estimation of SWS at higher frequencies (compared with CWS). The combination of the aforementioned criteria explains the conditions to obtain an overlapping spectral range between CWS and STL-SWEI. The SWS values obtained with both elastography modalities are similar to those reported in the literature from tissue mimicking phantoms (2–6.5 m/s) [12], [21], [37]–[39].

B. Lateral Resolution, Contrast, and CNR

With respect to lateral resolution, CWS presents better results (lower resolution values) when the V_f increases. This is

expected since shear waves have smaller spatial wavelengths. For STL-SWEI, it was found that as Δx increases, the lateral resolution has worse performance as expected. However, STL-SWEI can achieve better lateral resolutions when decreasing Δx . In that sense, the minimum lateral resolution from STL-SWEI is limited by its beamwidth (i.e., 0.8 mm).

It can be seen that for vibration frequencies higher than 340 Hz, CWS presents better lateral resolution, contrast, and CNR results than those obtained with STL-SWEI using Δx higher than 4 mm. However, in *ex vivo* and *in vivo* tissue, the attenuation is higher than that found in the phantoms. Thus, SWS estimation will be more difficult for higher vibration frequencies. Considering the *ex vivo* results in this work and other studies for *in vivo* tissue such as Zhang *et al.* [22], it can be seen that vibration frequencies higher than 300 Hz cannot be used. Therefore, using 300 Hz as the maximum operating V_f , results obtained with CWS are comparable to those obtained using STL-SWEI for Δx values between 3 and 6 mm.

In STL-SWEI, better lateral resolution and contrast were found as Δx decreases. However, worse CNR were obtained. In addition, the application of STL-SWEI in *ex vivo* and *in vivo* tissues will also be limited by the attenuation. Since the losses are worse with increasing Δx , it will be harder to track the induced shear waves. In this study, a $\Delta x = 3.04$ mm was used for the *ex vivo* beef liver tissue; in [29] a liver study was performed using a Δx equal to 5.31 mm. Considering the lateral resolution, contrast, CNR results, and the Δx value used in this study and in [29] for soft tissues, it can be said that comparable (with CWS) and reasonable SWS estimations will be obtained by applying a Δx range between 3 and 5.31 mm.

C. SWS and Accuracy Estimation in Ex Vivo Liver

Both modalities were able to measure SWS in *ex vivo* liver tissue with good correlation to MM. In this case, the frequency range was lower than that used for the phantom study due to the shear wave attenuation. Thus, it was not possible to generate interference patterns using CWS for higher vibration frequencies. It can be noted that the dispersion (i.e., SWS-frequency dependence) was higher for the *ex vivo* liver tissue than the gelatin-based phantoms used in this study, i.e., the estimated dispersion slope was 0.12 m/s per 100 Hz and 0.03 m/s per 100 Hz, respectively. Similar to the phantom experiments, CWS provides SWS values for lower frequencies than STL-SWEI. On the other hand, STL-SWEI could provide information at higher frequencies, where, for CWS, the cumulative attenuation loss across the 3–4 cm ROI is detrimental. Thus, this study shows the SWS behavior in a narrowband and broadband frequency range using CWS and STL-SWEI, respectively, and how it changes in gelatin-based phantoms and *ex vivo* liver tissue, which is a more viscoelastic material. Moreover, the SWS values obtained with both elastography modalities are similar to those reported in the literature for liver tissue (1–2 m/s) [9], [33]–[35], [40]. In that sense, this experiment increases the range of elasticity and SWS covered by CWS, STL-SWEI, and MM (i.e., 1–6 m/s). Finally, STL-SWEI has the advantage that it is not as time-consuming as CWS because it could provide

SWS results for different frequencies using the acquired data in one experiment.

D. Limitations of the Study

Some limitations of this study include the following. The CWS configuration used in this study may not be feasible for clinical implementation. Partin *et al.* [21] proposed the application of miniature surface sources for CWS generation which may develop into an achievable ultrasound-based device. STL-SWEI demonstrated its applicability for measuring the viscoelastic properties in soft tissue at a maximum depth of 4 cm [29]. Although this technique may be used for liver fibrosis staging as described in [18], further research is needed to evaluate STL-SWEI for clinical deployment at larger depths. Another limitation of this study is the need for testing in other tissues.

V. CONCLUSION

We have compared and characterized gelatin-based phantoms and *ex vivo* liver tissue using CWS and STL-SWEI and validated the results with MM. Although, they are expected to agree in perfectly linear, homogeneous, and isotropic materials, the SWS overlap is not guaranteed in all materials because each of the three methods have unique features, i.e., MM is a long time duration stress relaxation test applying a uniaxial constant strain, CWS is a sinusoidal steady state shear wave modality, and STL-SWEI is a transient broadband shear wave pulse technique. Nevertheless, the results using these modalities agree over an SWS range of 1–6 m/s. For each material, statistical analysis shows that the three modalities are not significantly different from one another.

The lateral resolution, contrast, and CNR could be measured using CWS and STL-SWEI. It was found that CWS and STL-SWEI give comparable lateral resolution, contrast, and CNR results for vibration frequencies less than 300 Hz and Δx values between 3 and 5.31 mm (which are reasonable parameters for soft tissue applications), respectively.

Finally, the results of this study contribute to the limited data currently available for comparing elastographic techniques, especially techniques that use different types of force to generate shear waves inside the material. Moreover, the methodology implemented in this document may be helpful for future standardization of different elastographic modalities.

ACKNOWLEDGMENT

The authors would like to thank J. Langdon for the implementation of the STL-SWEI.

REFERENCES

- [1] K. J. Parker, M. M. Doyley, and D. J. Rubens, "Imaging the elastic properties of tissue: The 20 year perspective," *Phys. Med. Biol.*, vol. 56, no. 1, p. R1, 2011.
- [2] T. Shiina *et al.*, "WFUMB guidelines and recommendations for clinical use of ultrasound elastography: Part 1: Basic principles and terminology," *Ultrasound Med. Biol.*, vol. 41, no. 5, pp. 1126–1147, 2015.
- [3] L. Castera and M. Pinzani, "Non-invasive assessment of liver fibrosis: Are we ready?" *Lancet*, vol. 375, no. 9724, pp. 1419–1420, 2010.
- [4] G. Ferraioli *et al.*, "WFUMB guidelines and recommendations for clinical use of ultrasound elastography: Part 3: Liver," *Ultrasound Med. Biol.*, vol. 41, no. 5, pp. 1161–1179, 2015.

- [5] R. G. Barr *et al.*, "Elastography assessment of liver fibrosis: Society of radiologists in ultrasound consensus conference statement," *Radiology*, vol. 276, no. 3, pp. 845–861, 2015.
- [6] P. Marcellin *et al.*, "Non-invasive assessment of liver fibrosis by stiffness measurement in patients with chronic hepatitis B," *Liver Int.*, vol. 29, no. 2, pp. 242–247, 2009.
- [7] L. Castera, "Hepatitis B: Are non-invasive markers of liver fibrosis reliable?" *Liver Int.*, vol. 34, no. s1, pp. 91–96, 2014.
- [8] D. Zhang *et al.*, "Comparison of acoustic radiation force impulse imaging and transient elastography for non-invasive assessment of liver fibrosis in patients with chronic hepatitis B," *Ultrasound Med. Biol.*, vol. 41, no. 1, pp. 7–14, 2015.
- [9] C. Cassinotto *et al.*, "Non-invasive assessment of liver fibrosis with impulse elastography: Comparison of supersonic shear imaging with ARFI and FibroScan," *J. Hepatol.*, vol. 61, no. 3, pp. 550–557, 2014.
- [10] L. Fan *et al.*, "Assessing liver fat fraction by ARFI induced shear wave attenuation: A preliminary result," in *Proc. IEEE Int. Ultrason. Symp. (IUS)*, Jul. 2013, pp. 17–20.
- [11] M. Muller, J.-L. Gennisson, T. Defieux, M. Tanter, and M. Fink, "Quantitative viscoelasticity mapping of human liver using supersonic shear imaging: Preliminary *in vivo* feasibility study," *Ultrasound Med. Biol.*, vol. 35, no. 2, pp. 219–229, 2009.
- [12] J. Oudry, T. Lynch, J. Vappou, L. Sandrin, and V. Miette, "Comparison of four different techniques to evaluate the elastic properties of phantom in elastography: Is there a gold standard?" *Phys. Med. Biol.*, vol. 59, no. 19, p. 5775, 2014.
- [13] T. J. Hall *et al.*, "RSNA/QIBA: Shear wave speed as a biomarker for liver fibrosis staging," in *Proc. IEEE Int. Ultrason. Symp. (IUS)*, Jul. 2013, pp. 397–400.
- [14] M. Palmeri *et al.*, "RSNA QIBA ultrasound shear wave speed Phase II phantom study in viscoelastic media," in *Proc. IEEE Int. Ultrason. Symp. (IUS)*, Oct. 2015, pp. 1–4.
- [15] J. Lobo *et al.*, "Prostate vibro-elastography: Multi-frequency 1D over 3D steady-state shear wave imaging for quantitative elastic modulus measurement," in *Proc. IEEE Int. Ultrason. Symp. (IUS)*, Oct. 2015, pp. 1–4.
- [16] R. Rojas, J. Ormachea, A. Salo, P. Rodríguez, K. J. Parker, and B. Castaneda, "Crawling waves speed estimation based on the dominant component analysis paradigm," *Ultrason. Imag.*, vol. 37, no. 4, pp. 341–355, 2015.
- [17] P. Song, M. W. Urban, A. Manduca, H. Zhao, J. F. Greenleaf, and S. Chen, "Comb-push ultrasound shear elastography (CUSE) with various ultrasound push beams," *IEEE Trans. Med. Imag.*, vol. 32, no. 8, pp. 1435–1447, Aug. 2013.
- [18] J. H. Langdon, E. Eleggbe, and S. A. McAleavey, "Single tracking location acoustic radiation force impulse viscoelasticity estimation (STL-VE): A method for measuring tissue viscoelastic parameters," *IEEE Trans. Ultrason., Ferroelectr., Freq. Control*, vol. 62, no. 7, pp. 1225–1244, Jul. 2015.
- [19] Z. Hah, C. Hazard, B. Mills, C. Barry, D. Rubens, and K. Parker, "Integration of crawling waves in an ultrasound imaging system. Part 2: Signal processing and applications," *Ultrasound Med. Biol.*, vol. 38, no. 2, pp. 312–323, 2012.
- [20] C. T. Barry *et al.*, "Shear wave dispersion measures liver steatosis," *Ultrasound Med. Biol.*, vol. 38, no. 2, pp. 175–182, 2012.
- [21] A. Partin, Z. Hah, C. T. Barry, D. J. Rubens, and K. J. Parker, "Elasticity estimates from images of crawling waves generated by miniature surface sources," *Ultrasound Med. Biol.*, vol. 40, no. 4, pp. 685–694, 2014.
- [22] M. Zhang *et al.*, "Congruence of imaging estimators and mechanical measurements of viscoelastic properties of soft tissues," *Ultrasound Med. Biol.*, vol. 33, no. 10, pp. 1617–1631, 2007.
- [23] Z. Liu and L. Bilston, "On the viscoelastic character of liver tissue: Experiments and modelling of the linear behaviour," *Biorheology*, vol. 37, no. 3, pp. 191–201, 2000.
- [24] L. S. Taylor, M. S. Richards, and A. J. Moskowitz, "Viscoelastic effects in sonoelastography: Impact on tumor detectability," in *Proc. IEEE Ultrason. Symp.*, vol. 2, Oct. 2001, pp. 1639–1642.
- [25] K. Hoyt, B. Castaneda, and K. J. Parker, "Two-dimensional sonoelastographic shear velocity imaging," *Ultrasound Med. Biol.*, vol. 34, no. 2, pp. 276–288, 2008.
- [26] K. Hoyt, T. Kneezel, B. Castaneda, and K. J. Parker, "Quantitative sonoelastography for the *in vivo* assessment of skeletal muscle viscoelasticity," *Phys. Med. Biol.*, vol. 53, no. 15, pp. 4063–4080, 2008.
- [27] B. Castaneda *et al.*, "Prostate cancer detection based on three dimensional sonoelastography," in *Proc. IEEE Ultrason. Symp.*, Oct. 2007, pp. 1353–1356.
- [28] E. C. Eleggbe and S. A. McAleavey, "Single tracking location methods suppress speckle noise in shear wave velocity estimation," *Ultrason. Imag.*, vol. 35, no. 2, pp. 109–125, 2013.
- [29] J. H. Langdon and S. A. McAleavey, "Single track location viscosity estimation by maximum likelihood estimation," in *Proc. IEEE Int. Ultrason. Symp. (IUS)*, Sep. 2014, pp. 991–996.
- [30] S. McAleavey, E. Collins, J. Kelly, E. Eleggbe, and M. Menon, "Validation of SMURF estimation of shear modulus in hydrogels," *Ultrason. Imag.*, vol. 31, no. 2, pp. 131–150, 2009.
- [31] S. A. McAleavey, "Analysis and measurement of the modulation transfer function of harmonic shear wave induced phase encoding imaging," *J. Acoust. Soc. Amer.*, vol. 135, no. 5, p. 2836, 2014.
- [32] N. C. Rouze, M. H. Wang, M. L. Palmeri, and K. R. Nightingale, "Parameters affecting the resolution and accuracy of 2-D quantitative shear wave images," *IEEE Trans. Ultrason., Ferroelectr., Freq. Control*, vol. 59, no. 8, pp. 1729–1740, Aug. 2012.
- [33] C. T. Barry *et al.*, "Mouse liver dispersion for the diagnosis of early-stage fatty liver disease: A 70-sample study," *Ultrasound Med. Biol.*, vol. 40, no. 4, pp. 704–713, 2014.
- [34] C. T. Barry *et al.*, "Shear wave dispersion in lean versus steatotic rat livers," *J. Ultrasound Med.*, vol. 34, no. 6, pp. 1123–1129, 2015.
- [35] K. J. Parker, "Experimental evaluations of the microchannel flow model," *Phys. Med. Biol.*, vol. 60, no. 11, p. 4227, 2015.
- [36] P. Song *et al.*, "Two-dimensional shear-wave elastography on conventional ultrasound scanners with time-aligned sequential tracking (TAST) and comb-push ultrasound shear elastography (CUSE)," *IEEE Trans. Ultrason., Ferroelectr., Freq. Control*, vol. 62, no. 2, pp. 290–302, Feb. 2015.
- [37] J.-L. Gennisson, A. Marcelan, A. Dizeux, and M. Tanter, "High frequency rheology of hybrid hydrogels using ultrasound transient elastography," in *Proc. IEEE Int. Ultrason. Symp. (IUS)*, Oct. 2012, pp. 2525–2528.
- [38] H. Latorre-Ossa, J.-L. Gennisson, E. De Brosses, and M. Tanter, "Quantitative imaging of nonlinear shear modulus by combining static elastography and shear wave elastography," *IEEE Trans. Ultrason., Ferroelectr., Freq. Control*, vol. 59, no. 4, pp. 833–839, Apr. 2012.
- [39] A. Maeva, M. Lee, and S. Foster, "Shear wave imaging at high frequencies: A feasibility study in tissue mimicking gelatin phantoms," in *Proc. IEEE Int. Ultrason. Symp. (IUS)*, Oct. 2012, pp. 2552–2554.
- [40] K. Rifai *et al.*, "Clinical feasibility of liver elastography by acoustic radiation force impulse imaging (ARFI)," *Digestive Liver Disease*, vol. 43, no. 6, pp. 491–497, 2011.



studies in the USA.

Juvenal Ormachea (S'14) was born in Lima, Peru, in 1987. He received the B.S. degree in electronics engineering and the M.S. degree in digital signal and image processing from the Pontificia Universidad Católica del Perú, Lima, in 2011 and 2015, respectively, and the M.S. degree in electrical engineering from the University of Rochester, Rochester, NY, USA, in 2016, where he is currently pursuing the Ph.D. degree in electrical and computer engineering.

Mr. Ormachea is a member of the IEEE UFFC. He received a Peruvian Scholarship for his doctoral



Roberto J. Lavarello (S'05–M'08–SM'13) was born in Lima, Peru, in 1978. He received the B.S. degree in electronics engineering from the Pontificia Universidad Católica del Perú (PUCP), Lima, in 2000, and the M.S. and Ph.D. degrees in electrical and computer engineering from the University of Illinois at Urbana–Champaign, Champaign, IL, USA, in 2005 and 2009, respectively.

He was a Postdoctoral Researcher with the University of Illinois at Urbana–Champaign from 2009 to 2011, where he conducted research in ultrasound. He is currently an Assistant Professor with the Sección Electricidad y Electrónica, PUCP. His current research interests include ultrasonic imaging, computational methods for acoustic propagation, quantitative ultrasound, and inverse problems with an emphasis on acoustical inverse scattering.

Dr. Lavarello is a member of the IEEE UFFC. He was a Fulbright Scholarship recipient from 2003 to 2005.



Stephen A. McAleavey (S'98–M'01) received the B.S. and M.S. degrees in electrical engineering and the Ph.D. degree in electrical and computer engineering from the University of Rochester, Rochester, NY, USA, in 1996, 1998, and 2002, respectively.

He was a Postdoctoral Research Associate in biomedical engineering with Duke University, Durham, NC, USA, from 2001 to 2004, where he contributed to the early development of ARFI imaging. In 2004, he joined as a Faculty Member with the Biomedical Engineering Department, University of Rochester, where he has continued to develop acoustic radiation force imaging techniques, for which he holds two patents, including spatially modulated ultrasound radiation force imaging, and other ultrasound imaging methods. He is currently an Associate Professor of Biomedical Engineering with the University of Rochester.



Kevin J. Parker (S'89–M'81–SM'87–F'95) received his B.S. (*summa cum laude*) degree in engineering science from The State University of New York at Buffalo, Buffalo, NY, USA, in 1976, and the M.S. and Ph.D. degrees in electrical engineering from the Massachusetts Institute of Technology, Cambridge, MA, USA, in 1978 and 1981, respectively, with a concentration in bioengineering.

He has held positions with the University of Rochester, Rochester, NY, USA, since 1981, where he is currently the William F. May Professor of Electrical and Computer Engineering, Radiology, and Biomedical Engineering. From 1998 to 2008, he was the Dean of the School of Engineering and Applied Sciences with the University of Rochester. His current research interests include medical imaging and linear and nonlinear acoustics.

Dr. Parker is a member of the Acoustical Society of America and the American Institute of Ultrasound in Medicine. He was named a Fellow of AIUM for his work on medical imaging and of ASA for his work on acoustics. He has received awards from the National Institute of General Medical Sciences in 1979, the Lilly Teaching Endowment in 1982, the IBM Supercomputing Competition in 1989, the World Federation of Ultrasound in Medicine and Biology in 1991, and the Joseph P. Holmes Pioneer Award from AIUM in 1999.



Benjamin Castaneda (S'02–M'04–SM'10) received the B.S. degree in electronics engineering from the Pontificia Universidad Católica del Perú (PUCP), Lima, Peru, in 2000, the M.S. degree in computer engineering from the Rochester Institute of Technology, Rochester, NY, USA, in 2004, and the M.S. and Ph.D. degrees in electrical and computer engineering from the University of Rochester, Rochester, in 2006 and 2009, respectively.

He has more than ten years of experience in the topics of image processing and its applications medical treatment and diagnostics. He is currently a Principal Professor with PUCP, being the Chief of the Medical Imaging Laboratory.

Dr. Castaneda received the SINACYT/CONCYTEC Award to the academic innovator for his work toward the development medical technology in Peru in 2013. In addition, in 2013, he won the National Inventions Contest in the patent category for his work dedicated to enhance the diagnostics of tuberculosis.